

Tunable and High Photoluminescence Quantum Yield from Self-Decorated TiO₂ Quantum Dots on Fluorine Doped Mesoporous TiO₂ Flowers by Rapid Thermal Annealing

Kamal Kumar Paul, Subhadip Jana, and P. K. Giri*

Herein a novel approach is reported to achieve tunable and high photoluminescence (PL) quantum yield (QY) from the self-grown spherical TiO₂ quantum dots (QDs) on fluorine doped TiO₂ (F-TiO₂) flowers, mesoporous in nature, synthesized by a simple solvothermal process. The strong PL emission from F-TiO₂ QDs centered at ≈ 485 nm is associated with shallow and deep traps, and a record high PL QY of $\approx 5.76\%$ is measured at room temperature. Size distribution and doping of F-TiO₂ nanocrystals (NCs) are successfully tuned by simply varying the HF concentration during synthesis. During the post-growth rapid thermal annealing (RTA) under vacuum, the arbitrary shaped F-TiO₂ NCs transform into spherical QDs with smaller sizes and it shows dramatic enhancement (≈ 163 times) in the PL intensity. Electron spin resonance (ESR) and X-ray photoelectron spectroscopy (XPS) confirm the high density of oxygen vacancy defects on the surface of TiO₂ NCs. Confocal fluorescence microscopy imaging shows bright whitish emission from the F-TiO₂ QDs. Low temperature and time resolved PL studies reveal that the ultrafast radiative recombination in the TiO₂ QDs results in highly efficient PL emission. A highly stable, biologically inert, and highly fluorescent TiO₂ QDs/flowers without any capping agent demonstrated here is significant for emerging applications in bioimaging, energy, and environmental cleaning.

past few years for their high aspect ratio (surface-to-volume ratio), distinctive physicochemical properties compared to the conventional nanostructures. Under equilibrium, {001} facet dominated TiO₂ nanostructure is rarely observed as it has very high surface energy (average surface energy of {001} facet (0.90 J m^{-2}) is double that of {101} facet (0.44 J m^{-2})).^[14] Thus, during the usual growth process, the less reactive {101} facet is dominated over the highly reactive {001} facet. However, several reports^[14–16] have been published on the controlled growth of TiO₂ single crystals with exposed {001} facet after the breakthrough work by Yang et al.^[17] that demonstrated the hydrothermal synthesis of anatase TiO₂ single crystals with 47% exposed {001} facet. Following this work, {001} facet dominated TiO₂ microcrystals are being extensively investigated with various doping and photocatalytic applications for environmental cleaning. Recently, mesoporous TiO₂ single crystals delivering enhanced mobility and optoelectronic device performance was reported by Crossland et al.^[18]

Ding et al. reported on mesoporous hollow TiO₂ microspheres with enhanced photoluminescence (PL).^[19] However, most of these works were carried out using a mesoporous template method and the PL yield was not addressed in these works. To the best of our knowledge, there is no report on fluorine doping of mesoporous TiO₂ nanostructure and the extremely high PL quantum yield (QY) of self-grown anatase fluorine doped TiO₂ (F-TiO₂) nanocrystals (NCs) on mesoporous F-TiO₂ flowers. Thus, a detailed study on structural and optical properties of mesoporous F-TiO₂ nanostructures is warranted to explore its novel properties including high PL QY.

With conventional semiconductor quantum dots, chiral quantum dots based cellular imaging, sensing, and biomedical applications are not so encouraging because of the involvement of toxic elements such as cadmium^[20] in the chiral composition. This hinders its applicability in living cells and study for nontoxic analogues of these chiral luminescent nanomaterials is of great interest.^[21] Recently, Cleary et al.^[22] reported on the highly luminescent TiO₂ nanoparticles (NPs) with chiral capping ligand having size 30–50 nm with a PL QY up to $\approx 3.5\%$. However, the reported PL yields were measured mostly in colloidal solution, where surface functionalization by the solvents

1. Introduction

Titanium oxide (TiO₂) is one of the most significant transition metal oxides and has been widely explored in photovoltaics,^[1,2] photocatalysis,^[3–5] sensors,^[6–8] Li-ion batteries,^[9–12] etc. Distinctive physical and chemical properties of TiO₂ facilitate such applications, depending on the morphology, surface feature, crystal phase, particle size, and exposed facets.^[13] Among different morphological features, 3D hierarchical architectures have opened up a wide research window in the

K. K. Paul, S. Jana, Prof. P. K. Giri
Department of Physics
Indian Institute of Technology Guwahati
Guwahati 781039, India
E-mail: giri@iitg.ernet.in

Prof. P. K. Giri
Centre for Nanotechnology
Indian Institute of Technology Guwahati
Guwahati 781039, India

 The ORCID identification number(s) for the author(s) of this article can be found under <https://doi.org/10.1002/ppsc.201800198>.

DOI: 10.1002/ppsc.201800198

may have contribution to the observed PL yield.^[23] Further, the TiO₂ nanostructures having size ≈100 nm is regarded as biologically inert and the reported TiO₂ nanostructure of size <100 nm may pose toxicity issue for the living cells.

Herein, we have grown mesoporous F-TiO₂ flowers in mixed phase by a simple and facile solvothermal method using Ti foil as the precursor material and dilute HF as the shape controlling agent. The as-grown F-TiO₂ flowers are uniformly decorated with the F-TiO₂ NCs of arbitrary shape. During rapid thermal annealing (RTA) under vacuum, the surface NCs transform into ultrasmall TiO₂ quantum dots (QDs) and it exhibits extremely high intensity PL emission (QY up to ≈5.76%) associated with shallow and deep trap states, which are further investigated by X-ray diffraction (XRD), Raman, electron spin resonance (ESR), and X-ray photoelectron spectroscopy (XPS) analyses. We discuss on the possible mechanism of shape evolution of the arbitrary shaped TiO₂ NCs to spherical QDs induced by RTA. Low temperature PL and time resolved PL studies enable us to elucidate the mechanism of high PL QY from the F-TiO₂ QDs/flowers.

2. Results and Discussion

2.1. Morphology Studies

2.1.1. Field Emission Scanning Electron Microscopy (FESEM) and EDS Analyses

The morphology and microstructural properties of the as-synthesized F-TiO₂ flowers were first studied by FESEM. **Figure 1** depicts the FESEM images of the systematic growth of TiO₂ NCs on the TiO₂ flower surface with the variation of HF concentration from 20×10^{-3} to 80×10^{-3} M, keeping the reaction duration fixed at 8 h. It is clear from **Figure 1a** that for the sample T20, the growth of symmetric TiO₂ flowers is complete, and the surface of each flower petal/component (truncated tetragonal pyramidal TiO₂ nanocrystal^[14]) is covered with uniform self-grown TiO₂ NCs due to the irregular surface etching by HF. Here due to selective etching, small sized NCs separated by nanosized pores are created on each surface. When the HF concentration increases from 20×10^{-3} to 40×10^{-3} M, the exposed highly reactive {001} surface gets etched selectively creating cavities on each {001} surface (see **Figure 1b**), while the {101} surface remains relatively smooth covered with TiO₂ NCs due to the less reactivity. After the post-growth heat treatment (RTA or furnace annealing) under vacuum, a major change in the surface feature of the TiO₂ flowers has been observed from FESEM. After vacuum RTA, the surface of T20 is transformed into mesoporous structure with very tiny NCs in between the pores, as shown in **Figure 1c**. The FESEM image of T40VR shown in **Figure 1d** depicts the cavity formation in {001} facet and overall mesoporous surface. **Figure S1a,b** (Supporting Information) shows a further magnified view of T20 surface confirming the self-growth of monodisperse TiO₂ NCs with arbitrary shape on the TiO₂ flower. When the HF concentration is further increased ($>40 \times 10^{-3}$ M), the cavity on the {001} facet becomes smaller and all the surfaces of the TiO₂ flowers get etched nearly uniformly irrespective of the nature of the facets and larger NCs are formed. Theoretical and experimental

studies on anatase TiO₂ have shown that surface energy (g) of {001} facet is greater than the {101} facet ($g_{\{001\}}$ (0.90 J m⁻²) $>g_{\{101\}}$ (0.44 J m⁻²)). Thus, {001} facet is more chemically active than {101} and it reacts with the HF faster, which creates the cavities on the {001} faceted TiO₂ surface. This results in the formation of TiO₂ NCs of arbitrary shape and size. It is observed that the size of the TiO₂ NCs becomes even larger with increasing the HF molar concentration (from 60×10^{-3} to 80×10^{-3} M) (see **Figure 1e,f**).

We have also monitored the growth of TiO₂ flowers with the variation of reaction duration from 4 to 16 h using 20×10^{-3} M HF solution as solvent (see **Figure S1** in the Supporting Information). An incomplete growth of TiO₂ flowers is observed for 4 h reaction (see **Figure S1c** in the Supporting Information), where the flower like structures start evolving. After 6 h of reaction, it is observed that the flowers are developed with truncated tetragonal pyramidal TiO₂ NCs and the flower size becomes larger, as shown in **Figure S1d** (Supporting Information). After 8 h of reaction, the growth of flowers is completed as shown in **Figure 1a**, where a uniform growth of the flower components in all directions with almost identical size is observed. Further increase in reaction duration leads to the overgrowth of the flowers. For 12 h of reaction, the number of truncated tetragonal pyramidal TiO₂ flowers growth increases and it starts fusing with each other (see **Figure S1e** in the Supporting Information). After 16 h of reaction, an excessive growth is observed and thus the TiO₂ flowers are fused with each other compactly giving it a spherical shape, see **Figure S1f** (Supporting Information). Similar to T20VR and T40VR, T60VR and T80VR also exhibit similar type of porous surface feature, as shown in **Figure S2a,b** (Supporting Information), respectively. But, the sample T20VR shows the optimal mesoporous nature with very tiny NCs uniformly distributed over the surface. After air RTA, T20 and T80 exhibit comparatively less mesoporous nature, which may be due to the lower density of O_v defects (see **Figure S2c,d** in the Supporting Information). During vacuum RTA, oxygen atoms may leave the bulk of the crystals and as a result Ov defects are created in high density, which may eventually form Ov clusters/voids inside the TiO₂ crystal.^[24] These voids may be responsible for the evolution of the mesoporous structure in TiO₂.^[25] Particularly, in case of vacuum RTA, the rapid change in thermal environment promotes coalescence of Ov defects and creation of voids as compared to the case of conventional annealing with slow heating/cooling rate. In case of air RTA, due to presence of excess oxygen, creation of void is not favorable and hence giving rise to less mesoporous structure.

To confirm the elemental composition and the doping, energy dispersive X-ray (EDX) spectra of the as-grown samples were recorded. **Figure S3** (Supporting Information) shows the EDX spectra of various as-grown TiO₂ flowers, which confirm the presence of Ti, O, and F in the nanostructures. In case of T10, TiO₂ has been formed with low density of oxygen vacancy (O_v) and with 3.5 at% of F (see **Figure S3a** in the Supporting Information). When the HF concentration is increased to 20×10^{-3} M, the concentration of F reaches to ≈7.5 at% with higher density of O_v (see **Figure S3b** in the Supporting Information). Further increase in HF concentration and reaction duration leads to the increase in O_v concentration, though the concentration of F in the samples remains almost unaltered

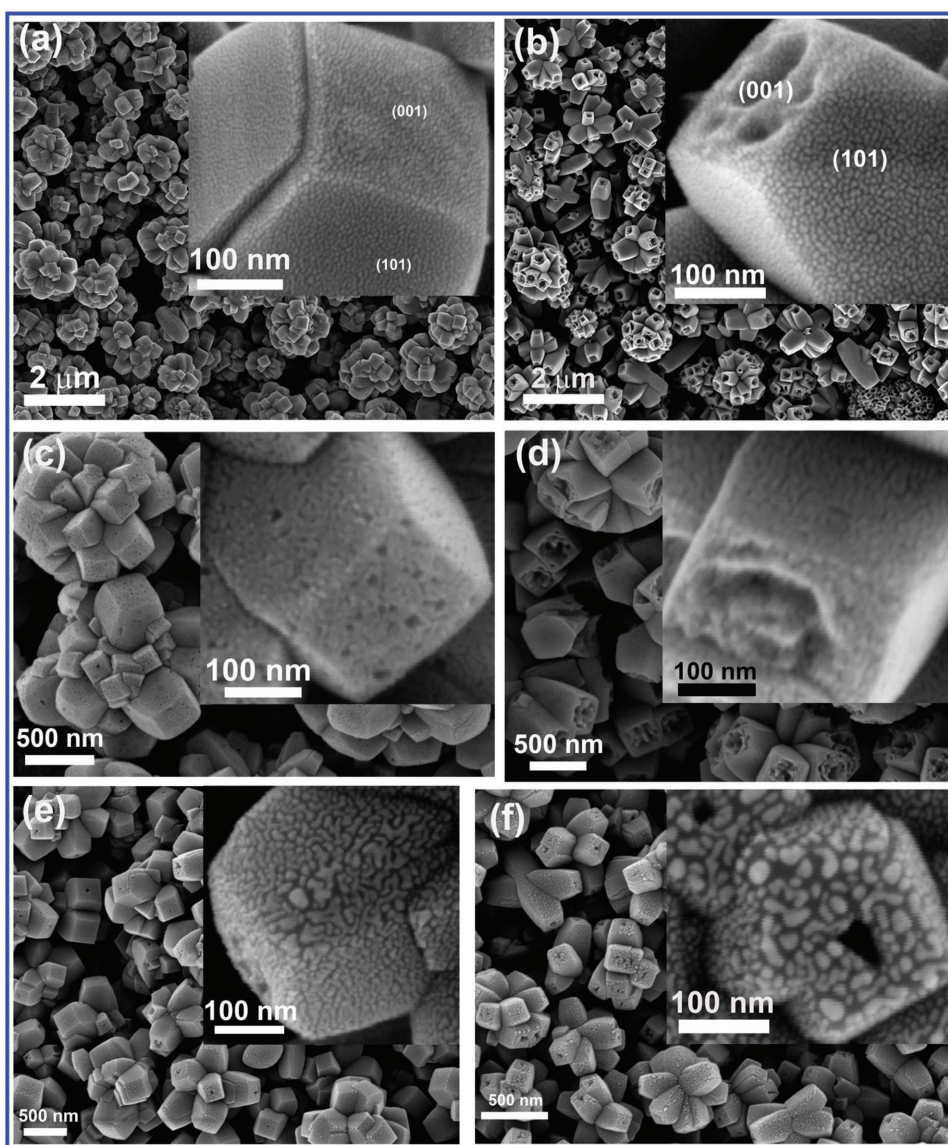


Figure 1. FESEM images of F-TiO₂ flowers: a) T20, b) T40; the inset in each case shows the enlarged view of the exposed facets of F-TiO₂ flower decorated with self-grown F-TiO₂ NCs. c,d) FESEM images of T20VR and T40VR, respectively. The inset in each case shows the magnified image revealing the mesoporous nature of the TiO₂ flower. e,f) FESEM images of F-TiO₂ flowers in T60 and T80, respectively. The inset in each case shows the magnified view of the mesoporous F-TiO₂ flowers decorated with self-grown F-TiO₂ NCs.

(see Figure S3c,d in the Supporting Information), which implies that the doping and surface adsorption of F ions reach to its optimum level beyond the 20×10^{-3} M HF concentration and 8 h of reaction duration. It is observed that after the vacuum annealing (RTA and furnace), the O_V density increases further, but the density of F ions decreases dramatically (see Figure S4 in the Supporting Information). The heat treatment at high temperature (600 °C) removes the F adsorbed on the surface of the TiO₂ flowers. In case of sample T20, after vacuum RTA the O_V density increases dramatically and reaches the highest value among all the samples (see Figure S4a in the Supporting Information). This effect is found to be less in the sample T20AR (air RTA, oxygen rich environment) (see Figure S4b in the Supporting Information). In case of furnace annealing, the O_V density increases from that of the untreated sample, but not

as high as in RTA treated sample (see Figure S4c,d in the Supporting Information). Thus, it is clear that the RTA treatment is superior over the normal furnace annealing to create controlled defects in the TiO₂ system.

2.1.2. Field Emission Transmission Electron Microscopy (FETEM) Analysis

To study the surface morphology and structure of F-TiO₂ flowers, FETEM images are acquired. Higher magnification FETEM image of T20 is shown in Figure 2a. During the growth, TiO₂ NCs of average size ≈ 5.0 nm (Figure S5a, Supporting Information) are observed to be grown by irregular etching on the TiO₂ flowers surface. Figure 2b shows the high-resolution

flowers. It can be noted that the lattice spacing for the TiO₂ NCs are calculated to be 0.33 nm, which corresponds to the (101) planes, while that of the truncated tetragonal pyramidal TiO₂ facet is 0.55 nm, which corresponds to the (001) planes. Figure 2j shows the FETEM image of T80VR and Figure 2k shows its enlarged view. It's clear that the truncated tetragonal pyramidal TiO₂ flowers are uniformly decorated with TiO₂ NPs having average size ≈ 12.8 nm (see Figure S5f in the Supporting Information). Figure 2l shows the high resolution lattice fringe pattern involving highly crystalline TiO₂ QD oriented along (004) planes grown on (101) facet of TiO₂ flower. The lattice d-spacing calculated here for all the cases is smaller than the standard value, which indicates a compressive strain in the sample, and this is consistent with the Raman and XPS analyses discussed later. The formation of spherical TiO₂ QDs from the arbitrary shaped TiO₂ NCs is induced here by the RTA treatment, which involves extremely fast change in the thermal environment of the sample. During the RTA treatment under vacuum, TiO₂ NCs with average size 5.0 nm (for T20) are observed to be transformed into spherical QDs with average diameter 4.2 nm, which falls in the weak quantum confinement regime^[26] and thus these ultraspherical NPs are referred as QDs. For T60 and T80, the NCs with average size 8.4 and 11.4 nm, respectively, are transformed into spherical NPs with sizes 9.7 and 12.8 nm, respectively after vacuum RTA (see Figure S5 in the Supporting Information). STEM elemental mapping analysis of T20 and T20VR also confirms the presence of Ti, O and F in the system, as shown in **Figure 3**. After RTA treatment, the concentration of F reduces greatly, though it does not vanishes completely, which may be due to the elimination of surface adsorbed F but not the F doped in the TiO₂ crystal lattice. It appears that F doped in the TiO₂ lattice has high thermal stability.

Now we attempt to explain the shape evolution of TiO₂ NCs from arbitrary shape into spherical NPs/QDs during the RTA treatment. In the classical nucleation theory,^[27,28] interface/boundary of the NCs plays an important role in the evolution of the NCs to a critical size. Classical nucleation theory predicts that to reduce the total free energy, size of the NCs may reduce/increase to arrive at the critical radius and spherical shape assumes a minimal surface area. Due to the thermal stress during the RTA process, the interfacial contact angle for the attached NCs increases when the shape evolves to spherical type and this helps in achieving the minimum free energy. In the present case, after 3 min vacuum RTA, we observe a remarkable shape evolution of self-grown TiO₂ NCs to perfect spherical shape in each case. This may be explained as follows. The melting point of the TiO₂ NCs reduces greatly as compared to its bulk form due to the formation of very small NCs. With the thrust of the thermal energy during RTA, the NCs tend to make a higher contact angle with the TiO₂ flowers interface to reduce the surface energy. Thus, the arbitrary shaped TiO₂ NCs transforms into the spherical QDs. Additionally, during the vacuum RTA, the concentration of O_v defects in the sample enhances dramatically, which induces compressive strain in the lattice that in turn squeeze the crystallite size of the TiO₂ QDs. Note that in case of normal furnace annealing, such a shape evolution to spherical QDs was not observed, implying the critical role of thermal stress during the RTA process in achieving the spherical NPs/QDs along with high defect density. Further, it has been reported that fluorine has an important role in controlling the faceted growth of TiO₂ nanostructures. Yang et al.^[29] reported that in absence of fluorine, no crystal facet control was observed for TiO₂ and only spherical polycrystalline anatase particles were formed. In this case, we noticed that after RTA, surface adsorbed fluorine is completely removed from the TiO₂ NCs, as revealed

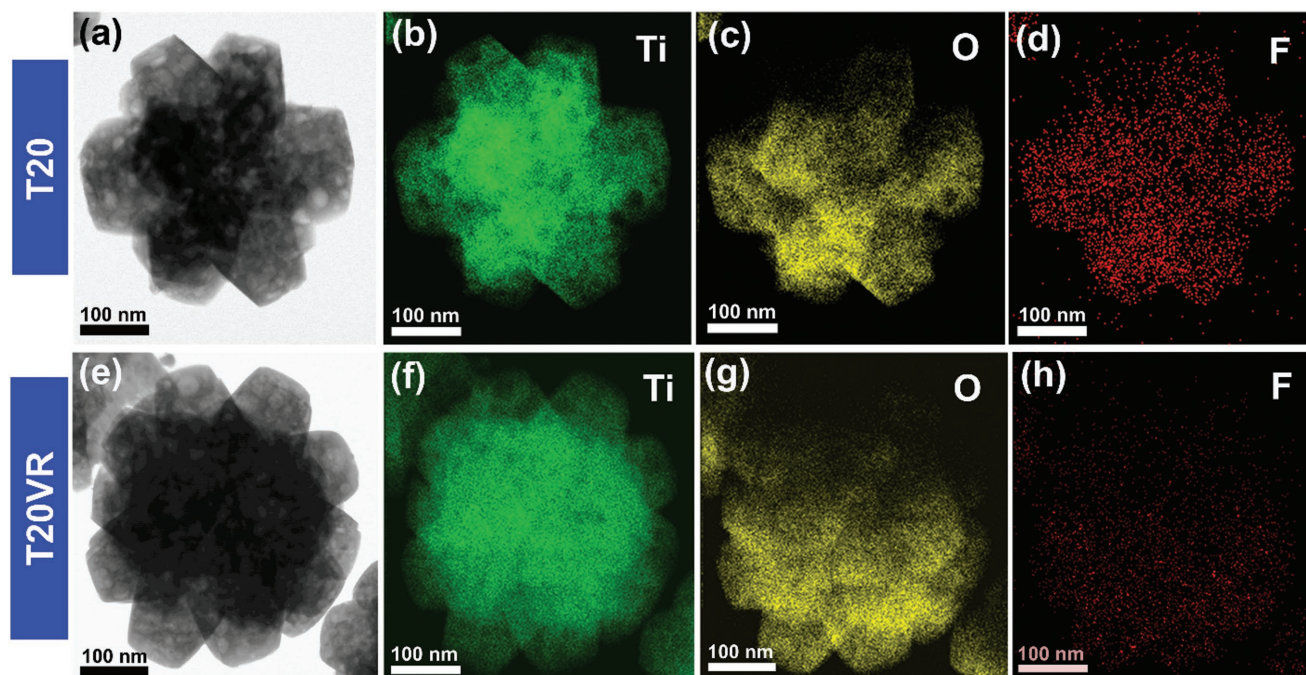


Figure 3. STEM images of mesoporous TiO₂ flowers and its elemental mapping in T20: a, d) as-grown, and e–h) after vacuum RTA.

from XPS results discussed later and this helps in achieving the growth of spherical TiO₂ NPs/QDs after annealing.

2.2. Structural Analysis

2.2.1. XRD Analysis

In order to confirm the crystal structure and phase of the F-TiO₂ flowers, XRD pattern of each sample has been recorded and the results are shown in Figure S6 (Supporting Information). All the diffraction peaks are very sharp clearly implying that the as-grown TiO₂ flowers are highly crystalline in nature. With increasing HF concentration or reaction duration, the peaks of Ti foil get diminished due to the higher density of flower growth, as shown in Figure S6a (Supporting Information). Most of the crystal planes of TiO₂ flowers correspond to pure anatase phase (JCPDS file # 782486) (marked as “A” in the figure). Besides the anatase phase, an additional monoclinic B-phase TiO₂ is detected at $2\theta \approx 44.59^\circ$ corresponding to (60-1) plane in all the samples.^[3] Another diffraction peak is detected at $2\theta \approx 47.94^\circ$, which can be assigned to either the A(200) TiO₂ (JCPDS file # 782486) or B(321) metastable brookite TiO₂ (JCPDS file # 761936). To investigate the effect of post-growth annealing, all the samples were treated at 600 °C under vacuum and air ambient. It is observed that after the annealing, the later peak is almost vanished (see Figure S6b in the Supporting Information). This implies that the corresponding brookite phase is not thermally stable. The peak intensity corresponding to brookite phase increases with increasing HF molar concentration as well as the reaction duration. It is observed

that the percentage of brookite phase increases almost linearly in both cases (see Figure S6c,d in the Supporting Information). After the heat (RTA and annealing) treatment, the most intense anatase (101) peak shows an upshift in Bragg angle ($\Delta 2\theta \approx 0.06^\circ$) along with a decrease in the FWHM. The upshift may be a signature of compressive strain in the lattice structure due to the defects in the lattice. After RTA treatment, the FWHM decreases, which implies an increase in crystallite size of the respective sample.

2.2.2. Raman Analysis

Figure 4a displays the Raman spectra of F-TiO₂ NCs/flowers grown at various HF concentrations. The inset shows a magnified view of the spectra along with that of the bulk TiO₂, which clearly reveals the peak shift and asymmetry in the Raman line shape. For the bulk TiO₂, the $E_g(1)$ Raman mode is detected at $\approx 142\text{ cm}^{-1}$ and observed to be symmetric in nature.^[30] It can be observed that for the sample T20 (Figure 4a), the most intense Raman peak is detected at $\approx 151.7\text{ cm}^{-1}$, which is $\approx 9.7\text{ cm}^{-1}$ blue shifted along with an asymmetry in higher wave number compared to bulk TiO₂. As this large blue shift is unlikely to originate from a single source, phonon confinement^[31] and nonstoichiometric defects^[32] and/or presence of brookite phase^[33] may contribute substantially to the observed blue shift.

For a clear understanding of the origin of asymmetry and large shift of the intense Raman peak, it is deconvoluted into two Lorentzian peaks; one centered at 147 cm^{-1} denoted as anatase E_{1g} and other centered at 156 cm^{-1} denoted as brookite^[34] (T20), as shown in Figure 4c. It is also observed that

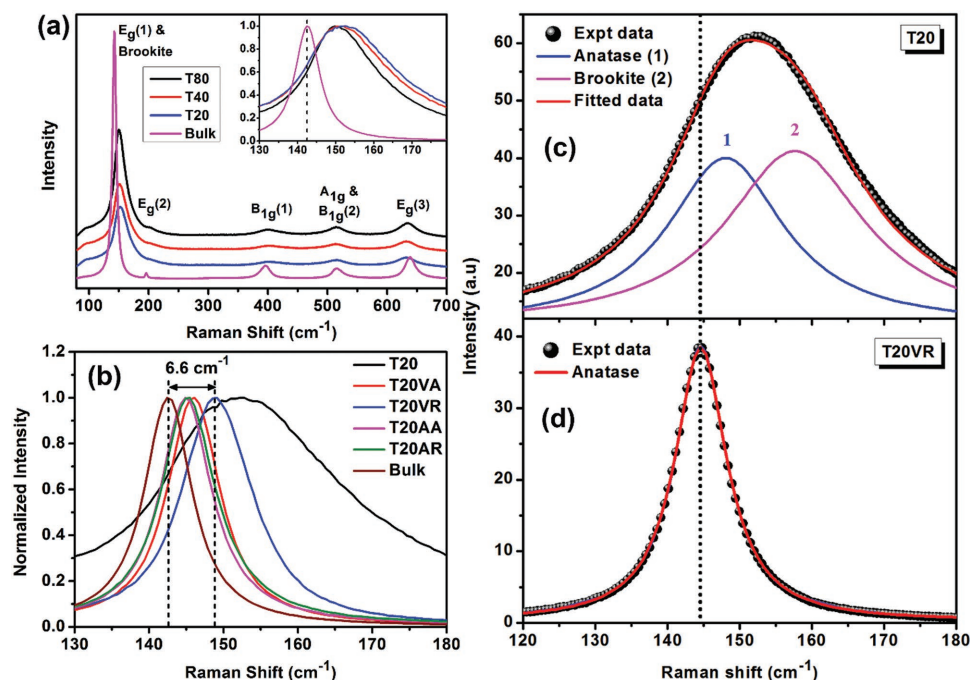


Figure 4. a) Raman spectra of F-TiO₂ flowers grown at various HF concentrations. Inset shows the normalized Raman spectra indicating large blue shift of $E_g(1)$ peak from that of the bulk TiO₂. b) Comparison of the normalized $E_g(1)$ peak for T20 before and after RTA/furnace annealing under different ambient. c,d) Lorentzian fit to the $E_g(1)$ peak in T20 before and after vacuum RTA, respectively. The vertical dotted line shows the peak shift and elimination of peak 2 after RTA.

the ratio of integrated intensity of brookite to anatase (brookite/anatase) phases increases with increasing molar concentration of HF as well as with the reaction duration (see Table S2 in the Supporting information), which is consistent with the XRD analysis. Thus, presence of brookite phase probably contributes to the large blue shift as compared to its bulk counterpart. Note that both the anatase and brookite peaks are blue shifted, partly because of the compressive strain induced in the lattice due to the oxygen vacancy, as evidenced from XRD, PL, ESR, and XPS analyses (discussed later). Note that TiO₂ flowers are covered with self-grown TiO₂ NCs of very small size (≈ 5.0 nm), which may result in the phonon confinement effect and asymmetry in the Raman line shape. It is further observed that with increasing HF concentration, the Raman band exhibits red shift with little asymmetry (see inset of Figure 4a) due to the formation of larger TiO₂ NCs (as confirmed from FESEM and FETEM). The decrease in FWHM implies the improvement in the crystallinity with increasing molar concentration of HF.

Interestingly, after the controlled heat treatment, the blue shift in the $E_g(1)$ peak is reduced and becomes symmetric in nature, which is due to the elimination of brookite phase and presence of only anatase phase (see Figure 4c,d), as evident from the XRD analysis. The reduced blue shift may be partly due to the reduction of lattice strain in the crystal. However, the $E_g(1)$ peak is still blue shifted with respect to that of the bulk, indicating the contribution of phonon confinement in the observed blue-shift. In case of T20, after vacuum RTA the blue shift is highest among differently processed samples and observed blue shift of 6.6 cm^{-1} (shown by pair of dashed line in

Figure 4b) may be contributed by phonon confinement and the oxygen vacancy defects in TiO₂ lattice. Note that after vacuum RTA of T20, the self-grown TiO₂ NCs size reduces and the arbitrary shape is transformed to spherical QDs with an average diameter ≈ 4.2 nm. Despite the fact that this size for TiO₂ falls in the weak confinement region for electron, we observe phonon confinement induced blue shift from these NPs/QDs.

2.2.3. XPS and ESR Analyses

Elemental composition, chemical valence state, surface defects, doping and strain in the F-TiO₂ flowers can be investigated by XPS study. Figure S7a (Supporting Information) shows the XPS survey spectrum of various F-TiO₂ flowers before and after different thermal treatments at 600 °C. XPS spectra show that the F-TiO₂ contains only Ti, O, and F elements and a trace amount of carbon. Each of the as-grown and annealed samples shows four symmetric Gaussian peaks in the Ti 2p XPS spectrum. Figure 5a shows the Ti 2p core level spectra of T20. The main two peaks at 458.8 eV (Ti 2p_{3/2}) and 464.5 eV (Ti 2p_{1/2}) are associated with the Ti⁴⁺ valence state, confirming the formation of TiO₂. The other two shoulder peaks at 457.3 eV (Ti 2p_{3/2}) and 460.2 eV (Ti 2p_{1/2}) are due to Ti³⁺ valence state, which is a signature of oxygen vacancy (O_v) defects in the system.^[3] The relative concentration of Ti³⁺ in the Ti 2p spectra was calculated as $\approx 9.2\%$ for both T20 and T80. Thus, it can be concluded that Ti³⁺ remains almost unaltered with the variation of HF molar concentration. However, after vacuum RTA, Ti³⁺ increases to

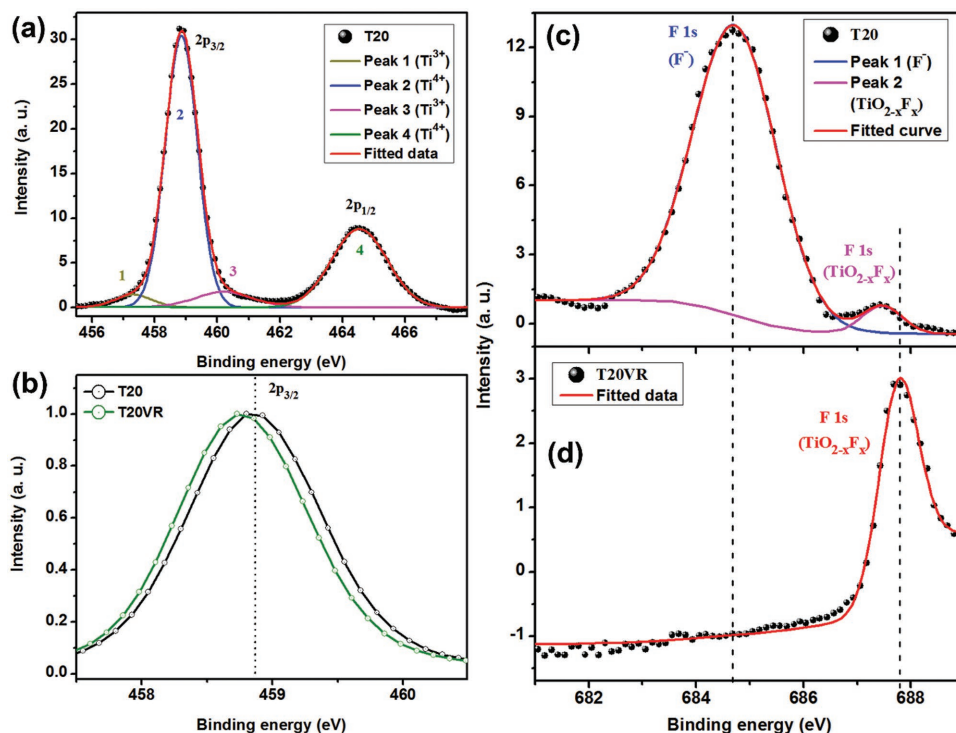


Figure 5. a) Ti 2p core level XPS spectrum of T20 with Gaussian fitting and Shirley baseline. b) Normalized Ti 2p_{3/2} XPS spectra of T20 and T20VR for comparison. The vertical dotted line is shown to visualize the peak shift after RTA. c) F 1s XPS spectrum and its Gaussian fittings for T20, with Shirley baseline. d) The F 1s XPS spectrum of T20VR fitted with a Gaussian peak, showing absence of lower energy F⁻ peak. The vertical dashed lines are shown to visualize the adsorbed and doped F positions before and after RTA.

9.5%, which indicates a minor increment in oxygen vacancy concentration, as shown in Figure S7c (Supporting Information). Figure 5b shows the normalized Ti $2p_{3/2}$ core level spectra of T20 sample before and after vacuum RTA. It can be noted that the peak at 458.8 eV corresponding to Ti^{4+} valence state, marked with a vertical dotted line, shifts to a lower binding energy, 458.7 eV after vacuum RTA. The shift to lower binding energy may be attributed to the lattice contraction.^[35] After the vacuum RTA treatment, decoration of self-grown TiO_2 NPs/QDs on the surface of the TiO_2 flowers was observed. Li et al.^[36] showed that the lattice contraction with decreasing particle size is thermodynamically favorable due to the higher surface curvature. One of the dominant phenomena governing the contraction in lattice volume with the reduction in particle size is the surface stresses due to the excess oxygen vacancy (as confirmed by XPS), which can create a positive pressure that in turn produces a lattice contraction.

To ascertain the doping of fluorine (F) in the TiO_2 system, high-resolution F 1s XPS spectrum of each sample was acquired and the results are presented in Figure 5c,d and Figure S7d (Supporting Information). Each of the F 1s spectrum of the as-grown samples is composed of two peaks, as shown in Figure 5c and Figure S7d (Supporting Information). The major peak located at ≈ 684.7 eV can be attributed to the F ions physically adsorbed on the surface of the TiO_2 flowers, while the other small peak located at 687.6 eV can be attributed to the substitutional F atoms in the TiO_2 lattice.^[37] The second peak originates from the F atoms doped into the TiO_2 crystal lattice during the hydrothermal process. Quantitative analysis shows that the relative percentage of doped fluorine increases

from 4.3% to 7.2% when the HF molar concentration increases from 20×10^{-3} to 80×10^{-3} M. Thus, it can be concluded that the doping concentration increases with increasing the molar HF concentration and with reaction duration as well. Figure 5d shows the high resolution XPS spectrum of T20VR. It is clear that the intense peak at ≈ 684.7 eV associated with the physically adsorbed F disappears completely after RTA, which signifies the complete removal of surface fluorine by thermal treatment. Interestingly, the only peak detected at 687.6 eV for T20VR is fully consistent with the doped F content in solid solution $TiO_{2-x}F_x$. The substitution of F for O^{2-} in the TiO_2 lattice is not too surprising as the atomic radii of F^- and O^{2-} ions are almost same. Interestingly, despite high temperature annealing, the doped F atoms remains inside the TiO_2 lattice and it strongly influences the optical properties of the NCs.

Figure 6a,b displays the O 1s spectra of F- TiO_2 synthesized with 20×10^{-3} and 80×10^{-3} M aqueous HF solvent, respectively. Each spectrum contains a long tail in the higher binding energy region making the spectrum asymmetric in nature and this tail implies the presence of impurities/defects in the sample. Each spectrum can be fitted with three symmetric Gaussian peaks, consistent with the literature.^[30] The most intense peak at 530.1 eV is attributed to the TiO_2 crystal lattice, while the additional peaks at ≈ 531.4 and ≈ 532.3 eV can be assigned to the Ti-O bond ($O_{Ti^{3+}}$) and adsorbed hydroxyl group at the surface of TiO_2 flowers, respectively.^[30] Additionally, one minor peak at ≈ 528.5 eV is seen for all the samples (see Figure 6a–c), which may be due to the subsurface oxygen atom adsorbed on the TiO_2 lattice.^[38] It is consistent with the fact that after vacuum RTA, this peak contribution is reduced (see Figure 6c),

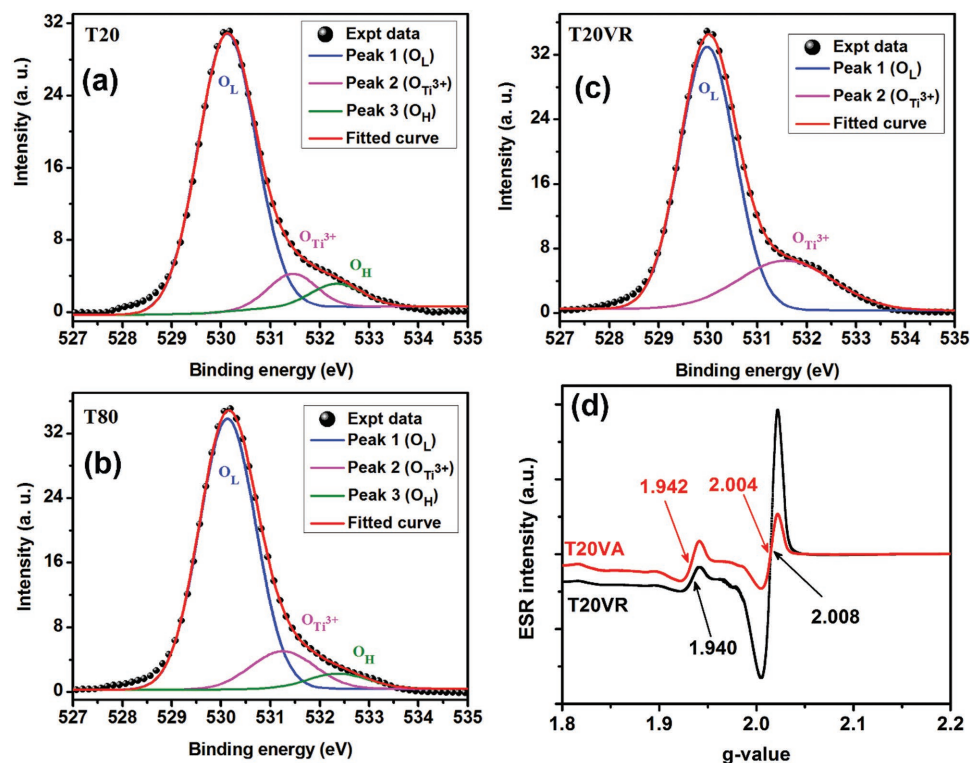


Figure 6. XPS O 1s spectra and its Gaussian fittings for a) T20, b) T80, with Shirley baseline. c) The XPS O 1s spectra with fitting for T20VR. d) Comparison of the room temperature ESR spectra for T20VR and T20VA. The respective g-values are indicated in each case.

due to the annealing in oxygen deficient environment. The relative concentration of $O_{Ti^{3+}}$ for the samples T20 and T80 has been calculated to be 8.5% and 12.9%, respectively. Thus, an enhancement in the concentration of O_V defects in the systems synthesized with higher HF concentration as well as reaction duration is confirmed, which is fully consistent with the PL results (discussed later). The O 1s spectrum of T20VR with two symmetric Gaussian deconvoluted peaks is shown in Figure 6c. It can be noted that the adsorbed hydroxyl group disappears from the sample due to the thermal treatment at high temperature (600 °C). The vacuum annealing enhances the concentration of oxygen vacancy defects greatly in the system. For the sample T20, the relative concentration of $O_{Ti^{3+}}$ has been calculated to be 22.4% and 24.3% after vacuum annealing and vacuum RTA, respectively. Though, both the RTA and furnace annealing were carried out under identical vacuum (1.5×10^{-2} mbar), RTA creates more oxygen vacancy defects in the system. It may be due to the thermal stress caused by the rapid change in the thermal environment during RTA, which creates more surface defects under reduced atmosphere. A summary of the relative concentration of Ti^{3+} , O_V and surface adsorbed F in various pre- and post-treated samples is shown in Table 1. It is evident that after post growth annealing, the adsorbed F atoms completely disappear and only the doped F atoms remain inside the TiO_2 crystal lattice.

ESR is a powerful tool to detect the spin polarized charge states in the defective TiO_2 nanostructure. ESR spectra of different samples are shown in Figure 6d. The samples T20VR and T20VA exhibit strong ESR signal at $g = 1.940$ and 1.942 , respectively, which confirms the presence of Ti^{3+} interstitial in the samples. Additionally, the ESR signals at g values of 2.008 and 2.004 are attributed to the singly ionized oxygen vacancy F^+ center for T20VR and T20VA, respectively.^[39] From the figure, it can be noted that in case of T20VR, the singly ionized oxygen vacancy defect (F^+ center) density is much higher than the Ti^{3+} and the F^+ species of other samples, which is fully consistent with the PL analysis. As compared to the post-annealed samples, the as-grown samples show negligibly low ESR signal as it contains very low density of defects. For the comparison, ESR signal of T20HR (RTA treatment under hydrogen gas atmosphere) was also recorded and the result is shown in Figure S7b (Supporting Information). Though it is showing signatures of both Ti^{3+} and F^+ centers, the signal intensity in T20HR is much lower than that of the T20VR sample. Thus, the T20VR contains higher density of F^+ center than the other samples.

Table 1. Summary of the relative percentage of Ti^{3+} , O_V , surface adsorbed F and doped F in various samples obtained from Ti 2p, O 1s, and F 1s XPS spectra, respectively.

Sample code	Ti^{3+} [%]	O_V [%]	Adsorbed F [%]	Doped F [%]
T20	9.2	8.5	95.7	4.3
T80	9.2	12.9	92.8	7.2
T20VA	11.5	22.4	0.0	0.4
T20VR	9.5	24.3	0.0	0.4
T20AA	9.3	18.2	0.0	0.3
T20AR	9.4	18.9	0.0	0.3

2.3. Optical Analysis

2.3.1. UV-Vis Absorption Study

The UV-vis diffused reflectance spectrum (DRS) is routinely studied to analyze the optical properties and band gap energy of nanostructured materials. The diffused reflectance of a system is related to the absorption coefficient by the Kubelka–Munk (K–M) function $F(R)$, given by the Equation (1)

$$F(R) = \frac{(1-R)^2}{2R} = \frac{\alpha}{S} \quad (1)$$

where α and S represent the absorption and scattering coefficients, respectively, and R is the reflectance of the sample. Figure 7a shows a plot of the K–M function of the pre- and post-treated samples corresponding to their reflectance spectra and Figure 7b shows the $(F(R)hv)^{1/2}$ versus hv plot for the calculation of effective band gap (indirect) of the F- TiO_2 flowers.

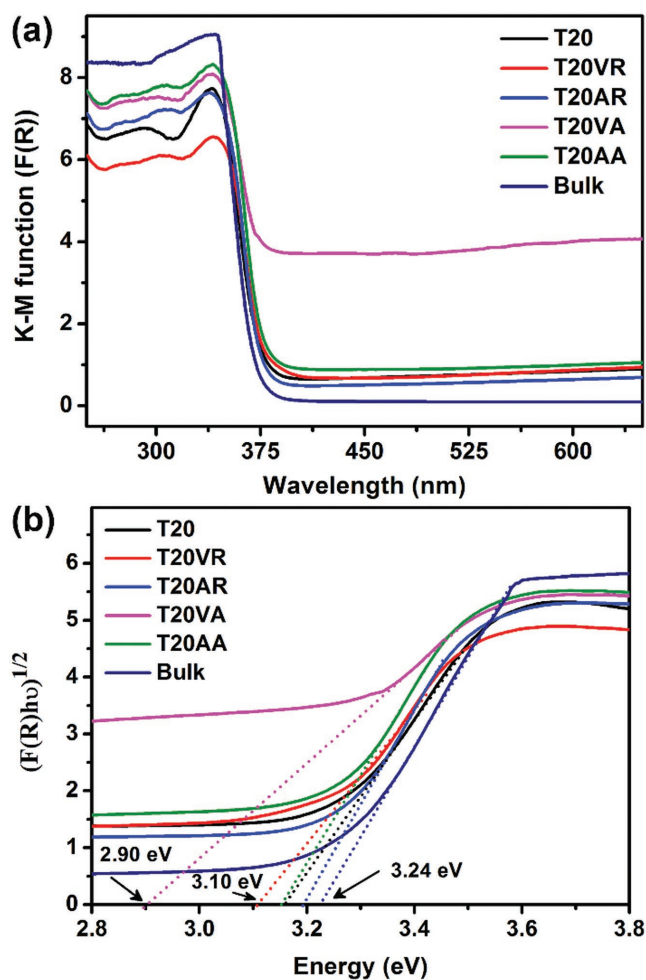


Figure 7. a) Kubelka–Munk plot, $F(R)$, derived from the diffuse reflectance spectra of T20 before and after annealing in different environments. The spectrum for the bulk TiO_2 is shown for comparison. b) Corresponding Tauc plot $[(F(R)hv)^{1/2}]$ vs hv plot considering the indirect band gap nature of the F- TiO_2 flowers. The effective band gap of different TiO_2 flowers is estimated from the intercept on the x-axis (extrapolated dashed lines).

Extrapolation of the linear portion of the graph to $(F(R)h\nu)^{1/2} = 0$ gives the effective band gap of the nanostructures. It is observed that the commercial bulk TiO_2 powder shows a band-edge absorption at ≈ 375 nm, which changes to ≈ 380 nm for the F- TiO_2 NCs/flowers. A marginally improved absorption is observed in the visible region for the as-grown sample. After vacuum RTA or furnace annealing, the surface adsorbed F disappears. However, the doped F along with the enhanced non-stoichiometric surface defects leads to the higher absorption in the visible region. On the other hand, after vacuum annealing, a dramatic enhancement in the absorption intensity in the visible region is noticed, which may be due to the high density of O_V defects, both on the flower and NC surface. The effective band gap for the corresponding sample (T20VA) is reduced to 2.90 eV, as shown in Figure 7b and Table 2. Therefore, after vacuum annealing, a narrowing of the band gap results in the visible light sensitization of F- TiO_2 flowers. This may be extremely beneficial for the efficient visible light photocatalysis. In case of T20VR, the whole absorption spectrum can be divided into three regions: up to 380, 380–420, and beyond 420 nm. Absorption up to 380 nm directly comes from the band to band transition, while the absorption in the range 380–420 nm arises due to the self-trapped excitons and shallow trap states Ti^{3+} centers. Santara et al.^[39] showed that the absorption in the range 420–580 nm (blue, green, and yellow region) can be attributed to the deep trap F^+ centers associated with the oxygen vacancies. Our results clearly show absorption beyond 420 nm, which can partly be due to the deep trap states, as confirmed from the PL analysis. The effective indirect band gap of

Table 2. Details of the surface features, band gap and PL quantum yield (QY) of different mesoporous F- TiO_2 nanostructures.

Sample code	Shape of self-grown TiO_2 NCs/QDs (size)	Band gap [eV]	PL QY [%]
T20	Arbitrary shape NCs (5.0 nm)	3.17	0.02
T60	Arbitrary shape NCs (8.4 nm)	3.17	0.07
T80	Arbitrary shape NCs (11.4 nm)	3.16	0.09
T20VR	Spherical QDs (4.2 nm)	3.10	5.76
T60VR	Spherical NPs (9.7 nm)	3.15	2.31
T80VR	Spherical NPs (12.8 nm)	3.14	2.73
T20VA	Arbitrary shape NCs	2.90	0.49
T20HR	Spherical QDs (4.5 nm)	3.15	0.21
Pure TiO_2 QDs	Spherical QDs (5.0 nm)	3.08	0.11

T20VR is calculated to be 3.10 eV, which is lower than that of T20. The reduction in the bandgap is believed to be caused by the high electron concentration induced by the oxygen vacancy defects in the TiO_2 NCs.^[40]

2.3.2. Photoluminescence Studies

In order to confirm the nature of defects and their dependence on the annealing environment, PL study was carried out. Figure 8a shows the room temperature PL spectra of F- TiO_2 NCs/flowers grown at different molar concentration of HF

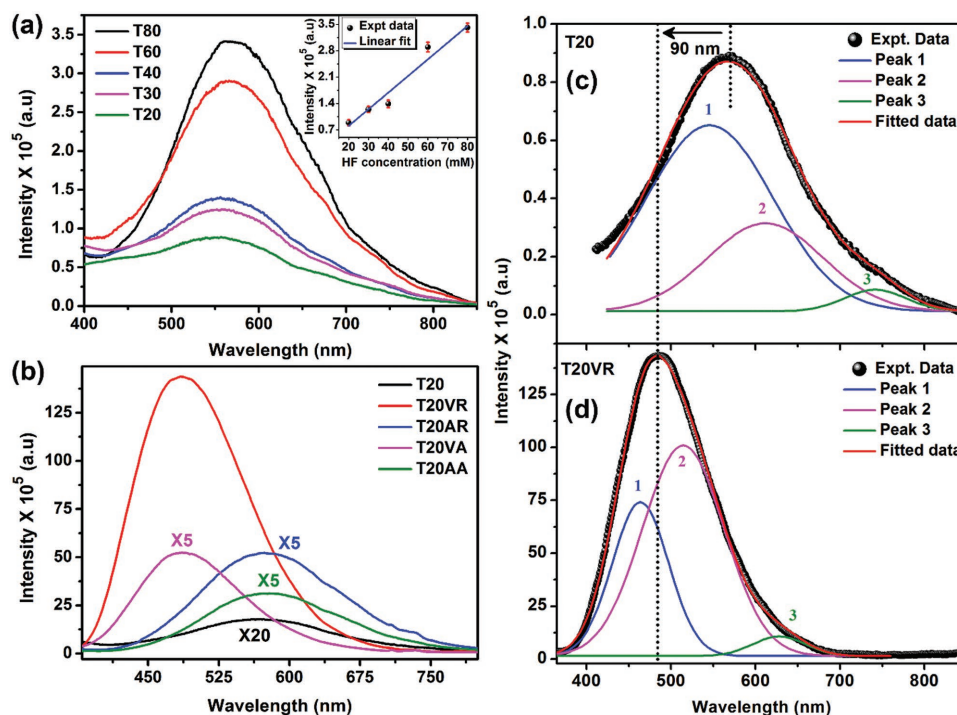


Figure 8. a) A comparison of the room temperature PL spectra (excited with 355 nm laser) of F- TiO_2 flowers prepared with different HF concentrations. Inset shows the variation of the PL intensity as a function of HF molar concentration along with the linear fit. b) A comparison of PL spectra of T20 before and after annealing in different ambient. The spectra with low intensity are shown in magnified scale, as indicated by the magnification factor in each case. c,d) Gaussian fit of PL spectrum for T20 and T20VR, respectively. The vertical dotted lines are shown to visualize the blue shift of peak after vacuum RTA.

under identical conditions of measurement. Due to the indirect band gap, no band edge emission was detected, and hence the possibility of free exciton recombination can be excluded. The observed broad visible PL band centered at ≈ 560 nm is primarily related to self-trapped excitons and oxygen vacancy defects in TiO_2 . PL intensity is found to be lowest for the sample prepared with lowest HF concentration, and the intensity increases linearly with increasing HF concentration, as shown in the inset of Figure 8a. PL intensity for 80×10^{-3} M HF is about 4 times higher than that of 20×10^{-3} M. Thus, the F-doping plays an important role in the PL emission efficiency of TiO_2 NCs. It is also observed that the PL intensity increases almost linearly with increasing the reaction duration, as shown in Figure S8a (Supporting Information).

After the post-growth annealing of F- TiO_2 flowers, a major enhancement in the PL intensity is observed. After the RTA/furnace annealing in air ambient, the PL intensity increases by ≈ 12 times and ≈ 7 times, respectively, without any major change in the nature of the spectrum. However, after RTA/furnace annealing under vacuum, a dramatic enhancement in PL intensity, blue shift (≈ 90 nm) and lower FWHM are observed for the PL peak. As compared to the as-grown sample, vacuum RTA treated sample (T20VR) shows more than two orders of magnitude enhancement (≈ 163 times) in the PL intensity, as shown in Figure 8b. Though all the vacuum RTA treated samples exhibit highly intense PL spectra, the T20VR sample shows the maximum enhancement in the PL intensity and it is about 5 times higher than that of T80VR. For the RTA treatment under vacuum, the size as well as the density of TiO_2 QDs and concentration of defects seem to be optimum in T20VR such that highest number of bound excitons are being generated and recombined, making it the most emission efficient.

For a better understanding of the origin of broad PL emission and giant enhancement in PL intensity after vacuum RTA, each spectrum is deconvoluted with multiple Gaussian peaks. The broad PL spectrum of as-grown sample (e.g., T20) could be fitted properly with three Gaussian peaks centered at 540 nm (peak 1), 625 nm (peak 2), and 745 nm (peak 3), as shown in Figure 8c.^[32,41] Peak 1 is ascribed to single electron trapped oxygen vacancy (F^+ center), peak 2 is related to the intrinsic defects in TiO_2 , may be induced by fluorine doping,^[41]

and peak 3 is likely to be due to the hydroxyl (OH^-) species, as confirmed from the XPS analysis. After RTA/furnace annealing in air, the PL spectrum can be again deconvoluted with three peaks, as shown in Figure S8 (Supporting Information) and the detailed fitting parameters are tabulated in Table S3 (Supporting Information). After vacuum RTA/furnace annealing, the PL spectra is shifted and it can be deconvoluted with three Gaussian peaks. Two major peaks observed at 464 nm (peak 1) and at 515 nm (peak 2) are related to oxygen vacancy related trap states. Peak 3 at centered 627 nm is related to the defects due to F-doping in TiO_2 (see Figure 8d for T20VR). Peak 1 corresponds to the emission from Ti^{3+} defect states, which is located just below the conduction band edge. Peak 2 corresponding to the 515 nm emission is due to deep trap states, which is associated with F^+ center, fully consistent with the ESR analysis. For sample in T20VA, the deconvoluted peak positions are similar to the sample T20VR as shown in Figure S8b (Supporting Information), with the details presented in Table S3 (Supporting Information). It can be noted that in both the cases, the integrated intensity corresponding to the F^+ center is calculated to be nearly double that of the Ti^{3+} center. XPS and ESR analyses confirm the higher defect density in T20VR, particularly for the TiO_2 QDs decorated on the TiO_2 flowers. Thus, it can be concluded that the RTA treatment under vacuum is superior to the normal furnace annealing for the optimization of radiative centers and high PL yield from TiO_2 NPs/QDs.

For the T20VR, the room temperature PL QY is measured to be 5.76%, which is significantly higher than that reported in the literature for TiO_2 nanostructures (QY ≈ 0.05 –3.5% or lower)^[22,23,42] The details of PL QY of our as-grown and annealed samples are tabulated in Table 2. Figure 9a shows the variation of PL QY for the samples grown with various HF concentrations (10×10^{-3} to 80×10^{-3} M) after 3 min vacuum RTA treatment, while Figure 9b exhibits the change in QY as a function of RTA duration for T20VR. It is clear that the sample T20VR grown with 20×10^{-3} M HF and subsequently vacuum RTA treated for 3 min is found to be optimized for the maximum PL QY. A variation in PL QY with the change in the solvothermal reaction duration has been shown in Figure S9a (Supporting Information) and T20VR with 8 h reaction is observed to be optimum. RTA treatment under hydrogen

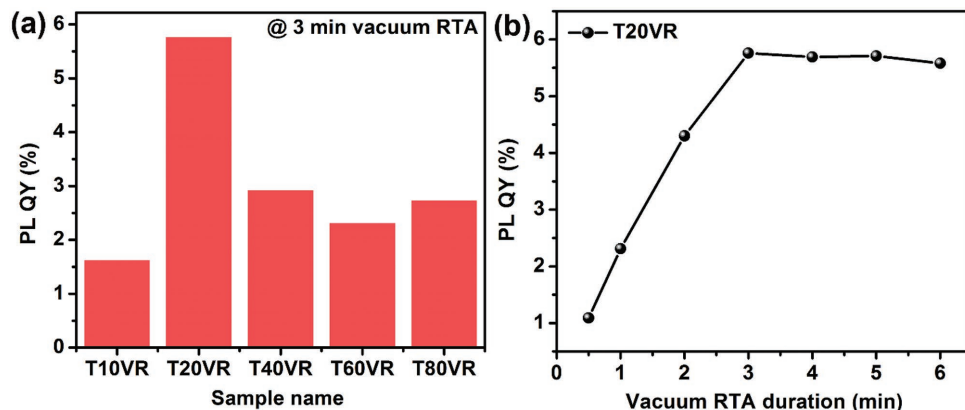


Figure 9. a) Comparison of the PL QY of vacuum RTA treated samples synthesized at various HF concentrations (10×10^{-3} to 80×10^{-3} M). b) PL QY as a function of duration of vacuum RTA for T20.

ambient was also performed to compare the QY and it shows a PL QY 0.21% (see Figure S9b,c in the Supporting Information). Note that the hydrogen annealed sample contains higher density Ti^{3+} species, but it does not show higher PL quantum yield compared to vacuum annealed sample, confirming the specific contribution of oxygen vacancy defects in the observed high PL QY. To understand the specific role of F^- doping and the interface of TiO_2 NCs/flowers in the PL enhancement, we prepared additional sets of bare TiO_2 QDs in purely anatase phase by sol-gel method and subsequently vacuum RTA treated for 3 min at the same temperature, see Figure S10 (Supporting Information). The sizes were chosen to closely match with that of the F- TiO_2 QDs prepared by the solvothermal method. The average sizes of the QDs here are ≈ 5.0 and ≈ 14.2 nm, as shown in Figure S10 (Supporting Information), along with the size distribution. However, these samples show much lower PL intensity with the highest QY of $\approx 0.11\%$ for smaller size QDs, as shown in Figure S9 (Supporting Information). Thus, the F-doping of the QDs and its attachment to the mesoporous F- TiO_2 flower are crucial to achieve the high PL QY from the mesoporous TiO_2 NCs/flowers. We believe that among the large number of samples studied here, T20VR is the best optimized sample offering highest PL QY.

Here, biologically inert F-mesoporous TiO_2 nanostructures (500–800 nm) without using any kind of capping ligand or imposing toxicity into the material have been demonstrated for the first time. For further evidence of the intense fluorescence and high quantum yield of self-grown TiO_2 QDs on TiO_2 flowers, fluorescence confocal microscopy imaging was carried out. Figure 10a shows the laser confocal microscopy fluorescence image of T20VR. The bright spots clearly demonstrate strong PL from the F- TiO_2 QDs/flowers. Since the QDs are uniformly decorated on the TiO_2 flowers, the PL image shows a flower like pattern in the magnified image shown in the inset of Figure 10a, due to the limitation of spatial resolution (120 nm) of this technique. The absence of a continuously bright/illuminated region in the image further signifies that the self-grown F- TiO_2 QDs are the primary emitting species in the TiO_2 flower. This result clearly shows

its suitability for bioimaging application as a fluorescent marker.

2.3.3. Time Resolved Photoluminescence Study

In order to investigate the lifetime and recombination dynamics of photogenerated charge carriers, time-resolved photoluminescence (TRPL) measurement was performed on T20VA and T20VR with 375 nm laser excitation and the PL emission was monitored at 520 nm. Figure 10b shows the TRPL decay profiles of T20VR and T20VA samples. It is evident that the PL decay rate is much faster in vacuum RTA sample as compared to that of furnace annealed sample. The TRPL decay profiles are fitted using a bi-exponential decay function expressed by the Equation (2), as follows

$$I(t) = \sum_{i=1}^2 A_i e^{(-t/\tau_i)} \quad (2)$$

where τ_i is the lifetime of i th components and A_i is the corresponding amplitude.

The average excited state lifetime can be calculated by using the following relationship^[43]

$$\tau_{av} = \frac{\sum_{i=1}^2 A_i \tau_i^2}{\sum_{i=1}^2 A_i \tau_i} \quad (3)$$

The details of the time constants (τ) of T20VR and T20VA are shown in the inset of Figure 10b. The biexponential fit suggests that mainly two distinct states contribute to the TRPL spectra in each sample, which is fully consistent with the steady state PL spectra. It can be noted that the average lifetime (τ_{av}) is considerably higher for the vacuum annealing case as compared to that of vacuum RTA. The τ_{av} of T20VR is found to be 1.20 ns, which is more than three times faster than that of T20VA sample ($\tau_{av} = 3.87$ ns). The lower τ_{av} in T20VR implies faster recombination and thus higher PL QY. The decay is monitored

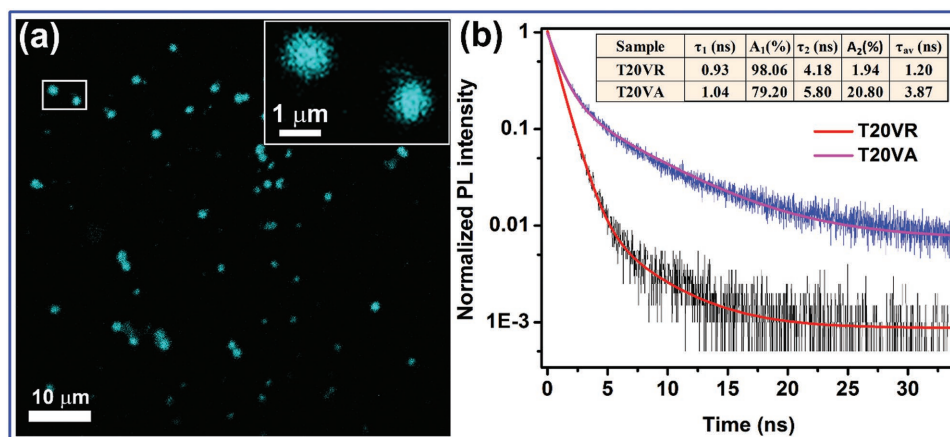


Figure 10. a) Laser confocal fluorescence microscope image of the TiO_2 flowers decorated with self-grown TiO_2 QDs in T20VR showing strong whitish fluorescence. Inset shows a magnified view of the fluorescent TiO_2 flowers. b) Comparison of the TRPL spectra of T20VR and T20VA, monitored at 520 nm (emission) with 375 nm excitation. The black and blue lines represent the experimental data, while the solid red and magenta lines represent the corresponding biexponential fit. The inset shows the details of lifetime (τ) components for different samples.

at 520 nm (emission wavelength), which is assigned to the F^+ (single electron trapped O_V) center. The contribution of F^+ center in the steady state PL spectra is observed to be $\approx 65\%$ for T20VR and $\approx 32.2\%$ for T20VA. This may be due to the much higher defect density in T20VR than in T20VA as confirmed from the ESR and PL analyses.

2.3.4. Temperature Dependent PL Study

In order to investigate the contribution of radiative and nonradiative processes, we have studied the temperature dependence of the PL spectra for T20VR, recorded in the range 80–300 K. It is observed that the intensity of the peak systematically increases with decreasing temperature, as shown in Figure 11a. The room temperature PL spectrum of T20VR has a broad peak centered at ≈ 485 nm (2.56 eV). With the decreasing temperature, it shows a slight red shift, as indicated by the vertical line (dashed) in Figure 11a. The vertical line indicates the peak position at ≈ 300 K. The inset of Figure 11a shows the variation of the integrated PL intensity as a function of temperature. At low temperature, the integrated PL intensity is much higher than that at room temperature. This is due to the activation of nonradiative recombination channels at room temperature, which results in the decrease in PL intensity. The temperature dependence of peak position and intensity could be ascribed to the interplay of radiative recombination of strongly localized excitons confined in the TiO_2 QDs and the temperature dependent nonradiative exchange interactions^[44] between electrons and holes via the defect states due to the nonstoichiometric oxygen vacancies. At any temperature T , the effective decay constant (τ_{eff}) of carrier is related to the radiative (τ_R) and nonradiative (τ_{NR}) lifetime of the transition from excited state to ground state by the equation

$$\frac{1}{\tau_{eff}(T)} = \frac{1}{\tau_R(T)} + \frac{1}{\tau_{NR}(T)} \quad (4)$$

Here, the variation of integrated intensity with temperature can be divided into two regimes: τ_R domination over τ_{NR} for $80 \text{ K} < T < 150 \text{ K}$ and τ_{NR} dominated for $T > 150 \text{ K}$. The transition from τ_{NR} domination to τ_R domination results in the red-shift of the peak center from ≈ 2.56 to ≈ 2.48 eV.

Additionally, the PL efficiency η_R can be calculated following the expression

$$\eta_R = \frac{1}{1 + \frac{\tau_R}{\tau_{NR}}} \quad (5)$$

It suggests that for $\tau_R \ll \tau_{NR}$, η_R approaches to unity, which indicates maximum possible efficiency of emission. On the other hand, if $\tau_R \gg \tau_{NR}$, $\eta_R \rightarrow 0$ (very small) and the light emission is very inefficient in this case.^[45] Thus, the necessary condition for the efficient luminescence is to be much shorter radiative lifetime than the nonradiative lifetime. In case of vacuum RTA treatment, the radiative lifetime (τ_R) is indeed found to be much shorter than the case of furnace annealing case. This results in extremely high PL QY (5.76%) for the

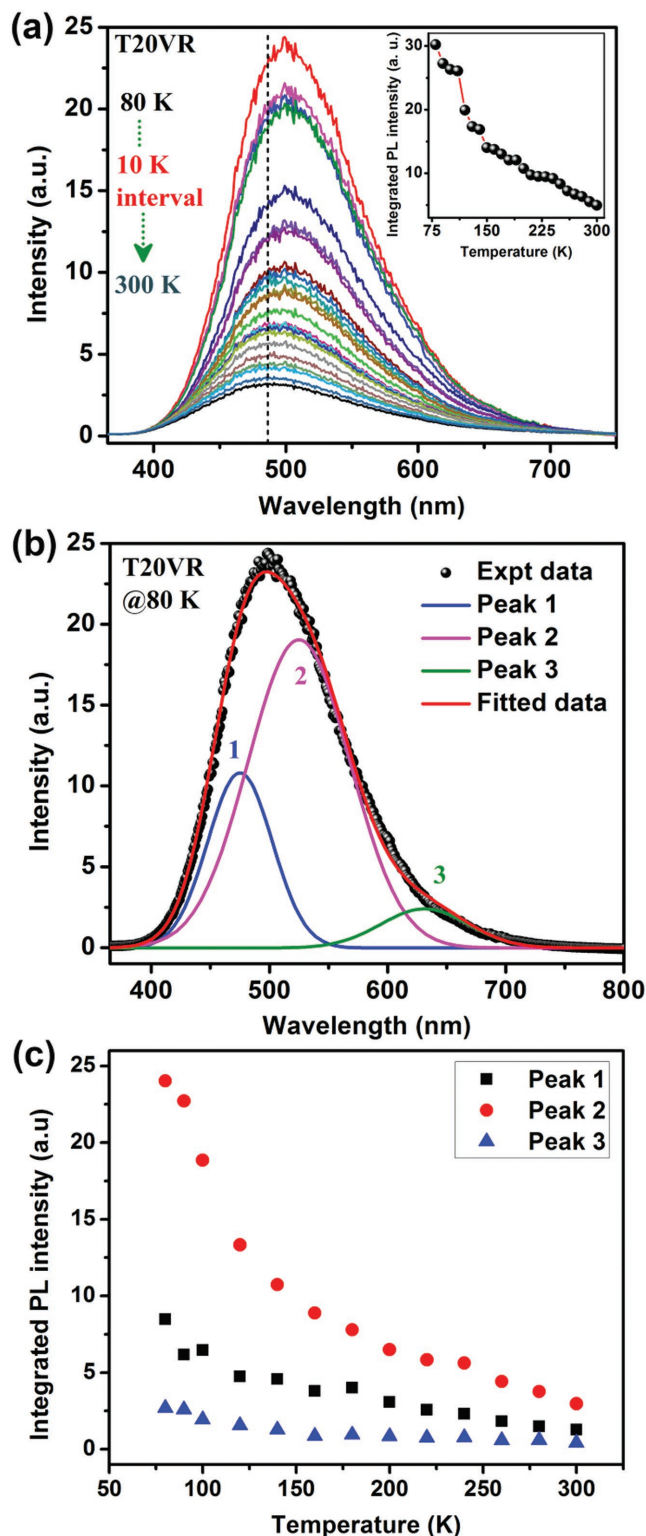


Figure 11. a) Low temperature PL spectra of T20VR at different temperatures. The vertical dotted line is shown to indicate the red-shift of the center of PL peak with lowering temperature. The inset shows change in integrated PL intensity as a function of temperature. b) Gaussian fit of PL spectrum of T20VR at 80 K. c) Change in integrated PL intensity of each peak as a function of temperature for sample of T20VR.

vacuum RTA sample (T20VR). Further, due to the size dependency of TiO₂ NCs on the radiative decay time, smaller size NCs tend to have much shorter life time. Hence, TiO₂ QDs with smaller size exhibits faster decay time and consequently the higher PL emission efficiency. Figure 11b shows the Gaussian fit of the PL spectrum of T20VR (centered at ≈500 nm) recorded at 80 K. The peak consists of three peaks (peaks 1, 2, 3) and change in relative intensity of each peak with temperature results in the shift of the mean position of the peak at lower temperature. Figure 11c shows a plot of the relative intensities (integrated) of each peak with temperature. Note that the change in PL intensity is more dramatic for peak 2 (F⁺ center)

and observed to be ≈2.8 times higher than that of peak 1. At lower temperature, more carrier relaxation from conduction band or Ti³⁺ state to F⁺ state is expected, since the capture cross section of F⁺ center is considered to be higher than that of Ti³⁺ state, which also may result in the ultrahigh efficiency of visible PL emission associated with the F⁺ center. Note that individual peak position remains nearly unchanged with temperature, the relative intensities changes substantially. Note that prior to the radiative recombination, the carriers may expend some of their energy in a multistep recombination process rather than a direct recombination to satisfy the energy and momentum conservation laws.^[45,46]

2.4. Mechanism of PL Enhancement in F-TiO₂ QDs/Flowers

After the RTA treatment, we observe the shape evolution of the arbitrary shaped self-grown TiO₂ NCs on the TiO₂ flowers to spherical TiO₂ QDs. For T20, vacuum RTA creates TiO₂ NPs/QDs with a mean size of ≈4.2 nm. Monticone et al.^[26] studied the quantum size effect of anatase TiO₂ NPs and found the exciton Bohr radius (r_{Bohr}) as 0.8 nm. They also showed that the weak confinement regime extends up to the size ≈8 r_{Bohr} , i.e., 6.4 nm even though no shift was observed in the band gap (or in the optical absorption edge) beyond the size $2r = 2$ nm.^[47] In the present case, ESR and XPS studies confirm the highest concentration of O_v defects in sample T20VR. As the size of the NPs are very small with high surface area and are uniformly distributed over the surface of TiO₂ flowers, the surface defects associated with oxygen vacancies are extremely high on the surface of TiO₂ NPs, which are almost covering the TiO₂ flower surface. Thus, the generation of surface defects by the vacuum RTA is mostly confined to the self-grown NPs and due to high electron density, the bandgap of TiO₂ NPs is slightly reduced. Consequently, the conduction band in the NP side tends to go little down as compared to that of flower side and the population density in the Ti³⁺ and F⁺ centers is extremely high. Self-grown highly defective TiO₂ NPs/QDs falling in weak confinement regime exhibits a 0.07 eV reduction in the effective band gap compared to its as-grown counterpart sample. Thus, instead of an enlarged band gap in TiO₂ QDs,^[48] a straddling type (type-I) band arrangement at the interface of flower and

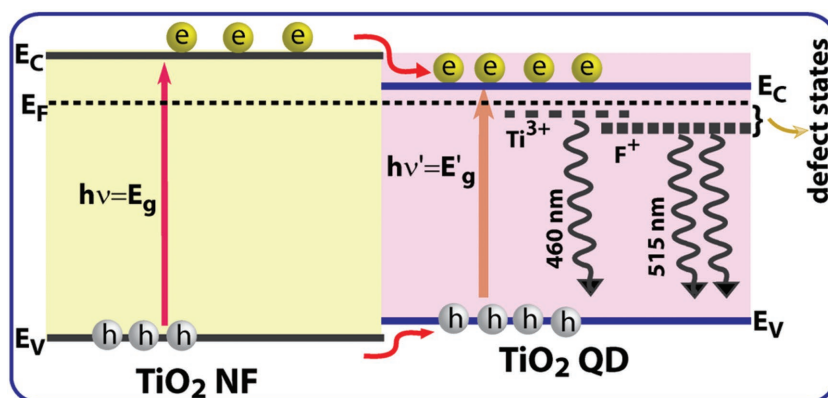


Figure 12. Schematic illustration of the PL mechanism mediated by different defects (Ti³⁺, F⁺ centers) in F-TiO₂ NPs/flowers in T20VR.

QD can be expected, as illustrated in Figure 12. With the laser excitation (355 nm), both the flower and NPs are excited and the straddling type band arrangement at the interface facilitates the migration of photo-excited charge carriers from the TiO₂ flower to NP side thermodynamically. Additionally, the electron capture cross section as well as defect density of F⁺ center may be higher and a relaxation of electron from conduction band as well as Ti³⁺ trap states to F⁺ center may be favorable in T20VR. As the decay time constant, τ , is inversely proportional to the defect density, the average excited state carrier life time associated with the transition from F⁺ state is much faster in T20VR than that in T20VA. This leads to ultrahigh intensity PL emission (QY ≈ 5.76%) from the T20VR with 65% emission from F⁺ center and 32% emission from the Ti³⁺ center. In the other sample (vacuum RTA treated), the size of NPs are much larger than that in T20VR, which leads to the lower surface coverage of flower and thus lower defect density in the NPs. Consequently the PL QY is lower for bigger NPs case, which happens for higher HF concentration as well higher reaction durations. Note that despite the presence of TiO₂ NPs/QDs, the band edge PL intensity was negligibly low in all the samples due to the indirect gap nature of the TiO₂. However, the defect mediated high yield and stable PL from the F-TiO₂ NPs is extremely important for its bioimaging and drug delivery applications.

3. Conclusion

In summary, we have successfully synthesized F-doped mesoporous TiO₂ nanostructure that is decorated with self-grown TiO₂ NCs with arbitrary shape. Effect of RTA and conventional furnace annealing on the shape evolution and PL quantum yield of these nanostructures reveal high PL quantum yield, despite its indirect band gap. The size distribution of NCs is successfully tuned by simply varying the HF concentration during solvothermal growth. Post-growth annealing increases the oxygen vacancy concentration, and it eliminates the surface adsorbed fluorine and metastable brookite phase from the system. Arbitrary shaped TiO₂ NCs on the surface of flowers grow irrespective of the facet surface energy due to the uniform etching by HF acid. The vacuum RTA treatment leads to enrichment of oxygen vacancy defects (O_v% ≈ 24.3%) in T20

sample and it transforms the arbitrary shaped TiO₂ NCs into ultrasmall spherical TiO₂ QDs, in order to minimize the free energy. In contrast, after conventional furnace annealing under identical condition, arbitrary shaped TiO₂ NCs remains on its surface with lower O_V concentration. Raman study reveals the role of phonon confinement and compressive strain in observed blue shift for the self-grown TiO₂ NCs on mesoporous TiO₂ flowers. After vacuum RTA, a major improvement in the PL was observed for different samples. We measured a PL QY of 5.76% for the optimized mesoporous F-TiO₂ QDs/flower. Confocal microscopy images show bright whitish emission from the F-TiO₂ QDs on TiO₂ flowers. Temperature dependent PL and time resolved PL studies reveal that the ultrafast radiative carrier lifetime on the F-TiO₂ QDs results in the highly efficient PL emission with record high PL QY. PL enhancement has been explained on the basis of the formation of type-I junction at the F-TiO₂ NP/flower interface, charge transfer from F-TiO₂ flower to F-TiO₂ QD side, carrier relaxation to surface defect states, high population density in the trap states (Ti³⁺ and F⁺ centers) and ultrafast carrier relaxation from the excited state. This study offers new insights in understanding the mechanism of ultrahigh PL emission by the F-TiO₂ NPs/QDs decorated on mesoporous F-TiO₂ flowers.

4. Experimental Section

Preparation of F-TiO₂ Flowers: Commercially procured titanium foil (Sigma Aldrich, purity 99.7%) was first degreased using acetone, 2-propanol, and then washed with deionized (DI) water. Afterward, the foil was cleaned by ≈18% aqueous HCl solution at 90 °C for 20 min to remove the oxide layer and impurities on its surface followed by DI water washing and finally dried in inert gas atmosphere. A 50 mL aqueous HF solution with various molar concentrations (10 × 10⁻³ to 80 × 10⁻³ M) was prepared and transferred to a Teflon-lined autoclave (Berghof, BR-100) along with the cleaned Ti foil. The sealed autoclave was heated and maintained at 150 °C for preselected times (2–16 h). After the hydrothermal treatment, the autoclave was allowed to cool down naturally. Then the foil was gently washed with DI water and dried in an oven at 80 °C.

Growth of F-TiO₂ QDs on F-TiO₂ Flowers: The as-grown F-TiO₂ flower sample was cut into pieces and subjected to RTA (Mila 3000P, ULVAC) at 600 °C for 3 min. During the RTA process, the heating and cooling rates were kept at 20 and 10 °C s⁻¹, respectively. RTA treatment was performed in three different ambient: ambient air, vacuum (≈1.5 × 10⁻² mbar) and hydrogen atmosphere.

Additionally, for comparison, some of the TiO₂ flower samples were annealed at 600 °C for 60 min in conventional tube furnace with heating and cooling rates at 5 °C min⁻¹. The furnace heat treatment was performed under ambient air and in vacuum (≈1.5 × 10⁻² mbar). A summary of the samples studied under different growth and processing conditions is provided in Table S1 (Supporting Information), with respective sample codes. The first part of the sample code refers to the HF concentration during growth and the second part refers to post treatment condition.

Characterization Techniques: The crystal structures of the samples were characterized by XRD (Rigaku RINT 2500 TTRAXIII, Cu Kα radiation). Crystallinity and phase composition of the as-synthesized flowers were measured by micro-Raman spectroscopy (LabRam HR800, Jobin Yvon). Morphologies of the samples were studied by FESEM (Sigma, Zeiss). The EDX spectra were recorded with the help of an X-ray detector (Oxford Instruments, UK) attached with a scanning electron microscope. The high-magnification surface morphologies and structures of the samples were studied by FETEM, HRTEM, and SAED pattern (JEOL-JEM

2100F operated at 200 kV). The UV–vis absorption spectroscopy was carried out using a commercial spectrophotometer (Shimadzu 2600). The room temperature steady state photoluminescence (PL) spectra were recorded using a 355 nm diode-pumped solid state (DPSS) laser excitation with the help of a fluorimeter (Fluoromax-4, Horiba Scientific) equipped with a PMT detector. The PL QY was measured using an integrating sphere (Horiba FM-sphere) incorporated with the Fluoromax-4 system. Fluorescence confocal microscopy was carried out using a laser scanning confocal microscope (LSM 880 microscope (Carl Zeiss)) with a laser excitation at 355 nm. Low temperature (80–300 K) PL measurements were made using a liquid nitrogen cooled optical cryostat (Optistat DNV, Oxford Instruments). XPS measurements were carried out with a photoelectron spectrometer (AXIS Supra, Kratos Analytical, UK) using Al Kα X-ray beam (1486.6 eV). Carbon 1s spectrum was measured each time for the calibration of the XPS spectra recorded for various samples. ESR measurements were done with a JEOL (JES-FA200) instrument operating in the X band. TRPL spectra were recorded in a picosecond time resolved luminescence spectrometer (Edinburgh Instruments, FSP920) with a time resolution of 50 ps.

Supporting Information

Supporting Information is available from the Wiley Online Library or from the author.

Acknowledgements

The authors acknowledge the financial support from MEITY (Grant No. 5(9)/2012-NANO (VOL-II)) for carrying out part of this work. Central Instruments Facility, I.I.T. Guwahati is acknowledged for providing the Raman, TEM, and FESEM facilities. A part of the reported work (XPS study) was carried out at the IITBNF, IITB under INUP which is sponsored by Deity, MCIT, Government of India. The authors thank Dr. Mukesh Singh, IITB for his invaluable support in the XPS measurement.

Conflict of Interest

The authors declare no conflict of interest.

Keywords

fluorine doped TiO₂ quantum dots, mesoporous TiO₂, photoluminescence quantum yield, rapid thermal annealing

Received: May 8, 2018

Revised: June 8, 2018

Published online:

- [1] Z. Sun, T. Liao, L. Sheng, L. Kou, J. H. Kim, S. X. Dou, *Chem. Eur. J.* **2016**, *22*, 11357.
- [2] P. V. Kamat, *J. Phys. Chem. C* **2012**, *116*, 11849.
- [3] K. K. Paul, R. Ghosh, P. K. Giri, *Nanotechnology* **2016**, *27*, 315703.
- [4] K. K. Paul, P. K. Giri, *J. Phys. Chem. C* **2017**, *121*, 20016.
- [5] K. K. Paul, P. K. Giri, *Encyclopedia of Interfacial Chemistry*, Elsevier, Oxford **2018**, pp. 786–794.
- [6] J. Bai, B. Zhou, *Chem. Rev.* **2014**, *114*, 10131.
- [7] S.-J. Bao, C. M. Li, J.-F. Zang, X.-Q. Cui, Y. Qiao, J. Guo, *Adv. Funct. Mater.* **2008**, *18*, 591.

- [8] G. Wang, Q. Wang, W. Lu, J. Li, *J. Phys. Chem. B* **2006**, *110*, 22029.
- [9] J. S. Chen, H. Liu, S. Z. Qiao, X. W. Lou, *J. Mater. Chem.* **2011**, *21*, 5687.
- [10] P. G. Bruce, B. Scrosati, J.-M. Tarascon, *Angew. Chem., Int. Ed.* **2008**, *47*, 2930.
- [11] D. Wang, D. Choi, J. Li, Z. Yang, Z. Nie, R. Kou, D. Hu, C. Wang, L. V. Saraf, J. Zhang, I. A. Aksay, J. Liu, *ACS Nano* **2009**, *3*, 907.
- [12] H. Xiong, M. D. Slater, M. Balasubramanian, C. S. Johnson, T. Rajh, *J. Phys. Chem. Lett.* **2011**, *2*, 2560.
- [13] W.-J. Ong, L.-L. Tan, S.-P. Chai, S.-T. Yong, A. R. Mohamed, *Nanoscale* **2014**, *6*, 1946.
- [14] M. Liu, L. Piao, W. Lu, S. Ju, L. Zhao, C. Zhou, H. Li, W. Wang, *Nanoscale* **2010**, *2*, 1115.
- [15] J. Miao, B. Liu, *RSC Adv.* **2013**, *3*, 1222.
- [16] Q. Xiang, J. Yu, M. Jaroniec, *ChemComm* **2011**, *47*, 4532.
- [17] H. G. Yang, G. Liu, S. Z. Qiao, C. H. Sun, Y. G. Jin, S. C. Smith, J. Zou, H. M. Cheng, G. Q. Lu, *J. Am. Chem. Soc.* **2009**, *131*, 4078.
- [18] E. J. W. Crossland, N. Noel, V. Sivaram, T. Leijtens, J. A. Alexander-Webber, H. J. Snaith, *Nature* **2013**, *495*, 215.
- [19] S. Ding, F. Huang, X. Mou, J. Wu, X. Lu, *J. Mater. Chem.* **2011**, *21*, 4888.
- [20] I. V. Martynenko, V. A. Kuznetsova, I. K. Litvinov, A. O. Orlova, V. G. Maslov, A. V. Fedorov, A. Dubavik, F. Purcell-Milton, K. G. k. Yu, A. V. Baranov, *Nanotechnology* **2016**, *27*, 075102.
- [21] S. Raphaël, W. Cécile, G. Hélène, B. Lavinia, L. Jacques, M. Christophe, *Nanotechnology* **2009**, *20*, 225101.
- [22] O. Cleary, F. Purcell-Milton, A. Vandekerckhove, Y. K. Gun'ko, *Adv. Opt. Mater.* **2017**, *5*, 1601000.
- [23] Y. Li, C. Song, Y. Wang, Y. Wei, Y. Hu, *Luminescence* **2007**, *22*, 540.
- [24] A. Folger, P. Ebbinghaus, A. Erbe, C. Scheu, *ACS Appl. Mater. Interfaces* **2017**, *9*, 13471.
- [25] Z. Su, Y. Zhu, Z. Wu, X. Peng, C. Gao, K. Xi, C. Lai, R. V. Kumar, *RSC Adv.* **2014**, *4*, 22989.
- [26] S. Monticone, R. Tufeu, A. V. Kanaev, E. Scolan, C. Sanchez, *Appl. Surf. Sci.* **2000**, *162–163*, 565.
- [27] J. K. Bording, J. Taftø, *Phys. Rev. B* **2000**, *62*, 8098.
- [28] N. T. K. Thanh, N. Maclean, S. Mahiddine, *Chem. Rev.* **2014**, *114*, 7610.
- [29] H. G. Yang, C. H. Sun, S. Z. Qiao, J. Zou, G. Liu, S. C. Smith, H. M. Cheng, G. Q. Lu, *Nature* **2008**, *453*, 638.
- [30] B. Santara, P. K. Giri, K. Imakita, M. Fujii, *Nanoscale* **2013**, *5*, 5476.
- [31] D. Bersani, P. P. Lottici, X.-Z. Ding, *Appl. Phys. Lett.* **1998**, *72*, 73.
- [32] K. K. Paul, P. K. Giri, *J. Phys. Chem. C* **2017**, *121*, 20016.
- [33] J. C. Yu, J. Yu, W. Ho, Z. Jiang, L. Zhang, *Chem. Mater.* **2002**, *14*, 3808.
- [34] M. N. Iliev, V. G. Hadjiev, A. P. Litvinchuk, *Vib. Spectrosc.* **2013**, *64*, 148.
- [35] B. Santara, P. K. Giri, K. Imakita, M. Fujii, *J. Phys. D: Appl. Phys.* **2014**, *47*, 215302.
- [36] G. Li, L. Li, J. Boerio-Goates, B. F. Woodfield, *J. Am. Chem. Soc.* **2005**, *127*, 8659.
- [37] G. Wu, J. Wang, D. F. Thomas, A. Chen, *Langmuir* **2008**, *24*, 3503.
- [38] T. E. Jones, T. C. R. Rocha, A. Knop-Gericke, C. Stampfl, R. Schlogl, S. Piccinin, *Phys. Chem. Chem. Phys.* **2015**, *17*, 9288.
- [39] B. Santara, P. K. Giri, K. Imakita, M. Fujii, *J. Phys. Chem. C* **2013**, *117*, 23402.
- [40] C. Dette, M. A. Pérez-Osorio, C. S. Kley, P. Punke, C. E. Patrick, P. Jacobson, F. Giustino, S. J. Jung, K. Kern, *Nano Lett.* **2014**, *14*, 6533.
- [41] D. Li, H. Haneda, S. Hishita, N. Ohashi, *Chem. Mater.* **2005**, *17*, 2596.
- [42] A. S. Susha, A. A. Lutich, C. Liu, H. Xu, R. Zhang, Y. Zhong, K. S. Wong, S. Yang, A. L. Rogach, *Nanoscale* **2013**, *5*, 1465.
- [43] M.-Z. Ge, C.-Y. Cao, S.-H. Li, Y.-X. Tang, L.-N. Wang, N. Qi, J.-Y. Huang, K.-Q. Zhang, S. S. Al-Deyab, Y.-K. Lai, *Nanoscale* **2016**, *8*, 5226.
- [44] R. Ghosh, P. K. Giri, K. Imakita, M. Fujii, *Nanotechnology* **2014**, *25*, 045703.
- [45] J. Zhang, X. Chen, Y. Shen, Y. Li, Z. Hu, J. Chu, *Phys. Chem. Chem. Phys.* **2011**, *13*, 13096.
- [46] A. V. Emeline, V. K. Ryabchuk, N. Serpone, *J. Phys. Chem. B* **2005**, *109*, 18515.
- [47] N. Satoh, T. Nakashima, K. Kamikura, K. Yamamoto, *Nat. Nanotechnol.* **2008**, *3*, 106.
- [48] L. Pan, J.-J. Zou, S. Wang, Z.-F. Huang, A. Yu, L. Wang, X. Zhang, *ChemComm* **2013**, *49*, 6593.